Composites Science and Technology 246 (2024) 110356

Contents lists available at ScienceDirect

Composites Science and Technology

journal homepage: www.elsevier.com/locate/compscitech

Highly conductive and mechanically robust MXene@CF core-shell composites for in-situ damage sensing and electromagnetic interference shielding

Yi Hu [a,b,c], Junzhen Chen [a,c], Guoyu Yang [a,c], Yujun Li [a,c], Ming Dong [b], Han Zhang [b], Emiliano Bilotti [d], Jianjun Jiang [a,c,**], Dimitrios G. Papageorgiou [b,*]

[a] School of Mechanical Engineering, Northwestern Polytechnical University, Xi'an, 710072, PR China
[b] School of Engineering and Materials Science, Queen Mary University of London, London, E1 4NS, UK
[c] Shaanxi Engineering Research Center for Digital Manufacturing, Xi'an, 710072, PR China
[d] Department of Aeronautics, Imperial College London, South Kensington, London, SW7 2AZ, UK

ARTICLE INFO

Handling Editor: Marino Quaresimin

Keywords:
MXene ($Ti_3C_2T_x$)
Carbon fiber reinforced resin matrix composites (CFRP)
Electrophoretic deposition (EPD)
In-situ damage sensing
Electromagnetic interference shielding effectiveness (EMI SE)

ABSTRACT

In this work, a new type of carbon fiber reinforced polymer (CFRP) composite was fabricated by introducing MXene nanoparticles onto the surface of carbon fibers (CF) *via* electrophoretic deposition (EPD) followed by thermal annealing. The MXene-reinforced CF/epoxy composites displayed enhanced mechanical properties and electrical conductivity as well as in-situ damage sensing capability. The uniformly deposited MXene nanoparticles contributed to a considerable enhancement of the flexural strength of CFRPs through hydrogen bonding and mechanical interlocking. The thermal annealing treatment reduced the amount of oxygen groups on the surface of MXene nanoparticles and enabled a 66 % increase of the out-of-plane electrical conductivity and a 20 % improvement of the electromagnetic interference (EMI) shielding effectiveness. The exceptional EMI performance of the core-shell hierarchical microstructure can be ascribed to the polarization of the inhomogeneous interfaces, the dipole polarization, and the conductive loss effect as a result of the presence of annealed MXenes on the surface of CFs.

1. Introduction

Electromagnetic pollution and electromagnetic interference (EMI) have become growing concerns in both aerospace and electronics fields due to the rapid development of electronic telecommunication technology [1–4]. High-performing, multifunctional EMI shielding materials are required to separate sensitive electronic instruments from mutual interference and protect humans from electromagnetic (EM) pollution. Conventional metals (e.g., Ag, Ti, and Cu) are widely used to shield against EM interference and pollution, due to their high electrical conductivity; however, they display several drawbacks such as difficulties in processability, susceptibility to corrosion, high-density-induced added weight, and rigorous coating techniques [5,6]. Quite significantly, the reflection-dominated EMI shielding mechanism of metals leads to a complete reflection of the incoming radiation. The inevitable subsequent production of secondary EM radiation then interferes with the regular operation of equipment that are present in the vicinity of the metal-based coatings [7–11]. Under such circumstances, it is critical to develop novel, high-performing EMI shielding materials to replace current metal materials used in such applications [12].

For applications within the aircraft, aerospace and other highly technical industries, light-weightiness is a prerequisite for employing materials as efficient EMI shields in an attempt to attribute energy efficiency and cost-effectiveness to the final structures [13,14]. It is well known that electrical conductivity is a key factor determining the EMI shielding property [15–18]. Consequently, low-density conductive polymer composites (CPCs) are ideal candidates to replace metals for EMI shielding applications. Porous polymer nanocomposite foams can achieve excellent EMI shielding effectiveness (SE) [19]. However, the majority of these conductive polymer foams are reinforced with high filler loadings, which commonly leads to severe nanoparticle aggregation, and ultimately to weak mechanical properties [20]. Intrinsically

* Corresponding author.
** Corresponding author. School of Mechanical Engineering, Northwestern Polytechnical University, Xi'an, 710072, PR China.
E-mail addresses: jianjun@nwpu.edu.cn (J. Jiang), d.papageorgiou@qmul.ac.uk (D.G. Papageorgiou).

https://doi.org/10.1016/j.compscitech.2023.110356
Received 8 April 2023; Received in revised form 19 October 2023; Accepted 17 November 2023
Available online 25 November 2023

conducting polymers (ICPs) can be also used for EMI shielding, owing to their low density and the highly desirable absorption-dominant shielding mechanism. However, the weak mechanical and thermal performance and poor processability, alongside their large costs, severely limit their practical application [2,17,21].

Considering that CF display low density (1.75 g/cm^3), high tensile modulus (700 GPa), superior chemical stability, outstanding thermal (1000 W/mK) and electrical conductivity (1.5 × 10^6 S/m) [22–24], CFRP composites should be used as lightweight structural materials that display excellent mechanical properties and outstanding EMI shielding performance [25]. Unfortunately, the inferior through-thickness properties of CFs currently limit significantly the application of CFRPs in multiple structural and EMI shielding operations [26]. In terms of structural behavior, the resin-rich regions that commonly exist between the fiber laminates weaken the mechanical properties of CFRPs, since stress is commonly concentrated at these areas where cracks initiate and then propagate without any obstruction [27–29]. In terms of the electrical properties of CFRPs, the insulating resin between CF layers inhibits the conductive path of fillers in the out-of-plane direction and substantially reduces the electrical conductivity [30]. Therefore, the fiber-matrix interface not only has a crucial impact on the mechanical performance of CFRP composites by transferring the stress efficiently, but it is key to the implementation of CFPRs in multifunctional applications [31–33].

In-situ damage sensing is also crucial for the CFRP composites. Although the commonly used acoustic emission and C-scan techniques are effective in detecting some parts of the damaged area (mainly close to the surface of the composite), the inability to differentiate between defects, the need for surface preparation and the high costs sometimes render them unsuitable for practical applications [34]. In comparison, internal embedded sensors that display continuous monitoring abilities and longer service life can be more effective. Electrical signal sensing can be optimized to could evaluate CFRP damage according to resistance or voltage changes. More interestingly, internal sensing accuracy could be enhanced by introducing conductive fillers into an electrically-insulating matrix or on the surface of anisotropically conductive reinforcements. In recent years, carbon nanotubes and graphene-related materials have been successfully incorporated into CFRP composites to realize damage detection [35,36]. However, the use of conductive MXene nanoparticles for the same purpose has not been investigated in detail. MXenes have proven to be highly promising materials for flexible strain sensors due to their properties [37]. Primarily, their high specific surface area enhances their ability to detect changes in their surroundings, concurrently affording substantial surface area for the accommodation of target loading [38]. Additionally, MXenes offer flexibility in surface functionalization, as they have a rich surface chemistry that can be easily modified with various functional groups. This allows enhancement of their interactions with specific types of damage (such as tensile damage [39,40], low-velocity impact and high velocity impact damage [41], shockwave damage [42] et al.), facilitating selective target detection [43,44]. MXenes can display metal-like electrical conductivity, reaching levels as high as 24,000 S/cm [45]. This conductivity can be finely tuned by adjusting MXene composition and surface functionalization, which are highly important features for designing sensors with customized sensitivity thresholds [46,47]. Finally, MXenes exhibit remarkable chemical stability, granting them resilience in challenging detection environments and in the presence of potentially corrosive substances [48]. While carbon nanotubes and graphene also offer distinct benefits towards multifunctionality, MXenes possess a significant advantage in the field of damage detection applications due to their adjustable electrical conductivity and flexibility in surface functionalization.

Electrophoretic deposition (EPD) is of the most effective strategies to improve the mechanical properties [30,49] and electrical conductance [50,51] of fiber-reinforced composites by optimizing the interface between the fiber and the matrix. However, most literature works have focused on the deposition of carbon nanotubes and graphene nanoplatelets on fibers [52,53]. The influence of high performing, multifunctional MXene nanoparticles on the mechanical and electrical properties of CFRP composites *via* the EPD method is still in its infancy.

This present work is focused on the fabrication of a highly conductive and mechanically robust CFRP composite for effective in-situ damage sensing and EMI shielding by homogeneously coating MXene nanoparticles onto the CF surface. The effect of a post-EPD thermal annealing process on the mechanical and electrical properties of CFs was also analyzed. Vacuum-assisted resin infusion (VARI) was adopted to inject the epoxy resin into the MXene/CF preform and fabricate multifunctional CFPR structures. Mechanical tests, electrical conductivity measurements, and EMI shielding experiments were conducted to characterize the related mechanical, electrical, and electromagnetic properties.

2. Materials and methods

2.1. Materials

The CF fabric (T300, 12K, plain woven) was purchased from Toray. Epoxy 5015 resin and curing agents were obtained from Sino Composite Co., Ltd. Ti_3AlC_2 powders of 400 mesh were bought from Fo Shan Xin Xi Technology Co., Ltd. Lithium fluoride (LiF) and magnesium chloride hexahydrate ($MgCl_2 \bullet 6H_2O$) were purchased from Aladdin Biochemical Technology Co., Ltd. Nitric acid and hydrochloric acid were provided by Sinopharm Chemical Reagent Co., Ltd. All chemicals were directly used without further purification.

2.2. Preparation of $Ti_3C_2T_x$ and pretreatment of CF

The synthesis of $Ti_3C_2T_x$ took place according to the process described by Chae et al. [54]. Desizing and oxidizing treatments were sequentially employed to remove impurities from the CF surface and introduce active functional groups. For the desizing process, the CFs were washed in boiling acetone continuously for 48 h at 60 °C. The oxidization process was conducted by soaking the desized CF in nitric acid for 6 h at 80 °C. The desizing and oxidizing processes were followed by repeated washing with deionized water to remove the residual acetone and nitric acid. Finally, drying was conducted under vacuum at 100 °C for 2 h. From this point onwards, the CF materials in this paper refer to the carbon fibers pretreated sequentially by desizing and oxidizing processes.

2.3. Electrophoretic deposition of $Ti_3C_2T_x$ onto CFs

A schematic of the EPD setup is shown in Fig. 1. The CF fabric had copper glued on its four edges and acted as the cathode. A plate of graphite was used as an anode. The EPD suspension was fabricated by dispersing the MXene nanoparticles and magnesium chloride hexahydrate into deionized water, followed by agitation and ultrasonication. The magnesium chloride hexahydrate was used to enhance the conductivity of the suspension and produce the positively charged MXene nanoparticles. The final suspension concentration was 0.125 mg/mL with equivalent MXene and magnesium chloride hexahydrate content. The distance between the cathode and anode was set at 2 cm. The applied voltage between the two electrodes was 20 V, and the electric field was kept constant for 30 minutes to complete the EPD process. The optimization of the EPD process took place in our previously published work [56]. Furthermore, ultrasonication was adopted to remove bubbles produced during electrolysis and prevent agglomeration of MXene nanoparticles. An ice bath was also used to protect MXenes from oxidation due to the heat produced during ultrasonication. The fabric weight was measured before and after the EPD process and the MXene mass fraction on the CF fabric was found to be 13 wt%.

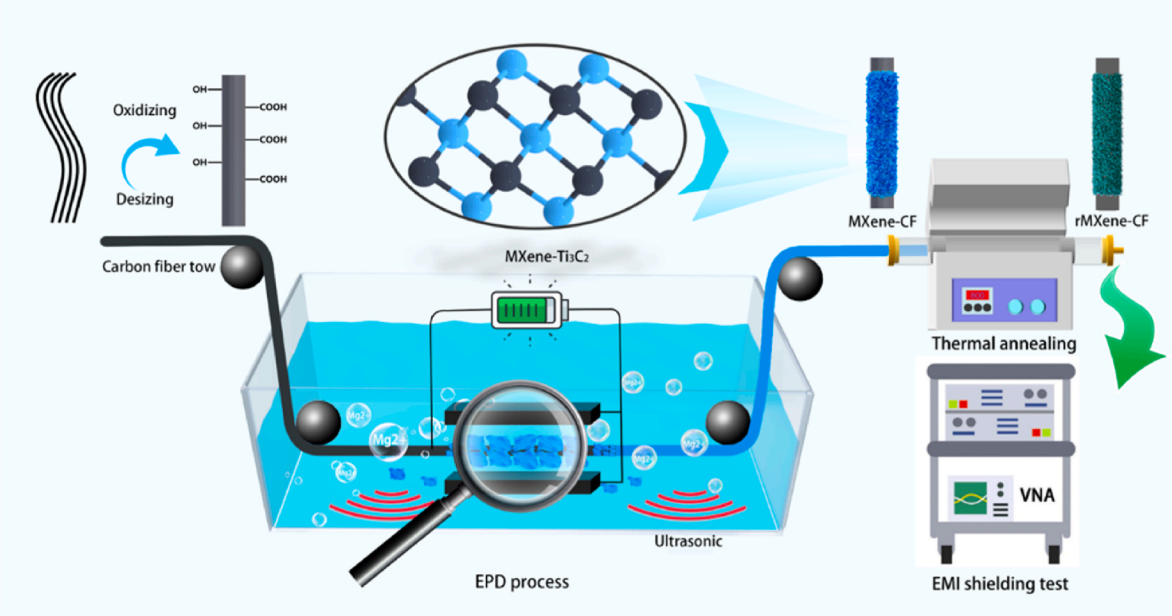

Fig. 1. Illustration of the modification of CF fabric *via* EPD of MXenes and the following thermal annealing treatment as well as the VNA test process.

2.4. Thermal reduction of MXene-deposited CFs

The rMXene-CFs (where r stands for reduced) were pretreated *via* a thermal annealing process to enhance the electrical conductivity of MXene nanoparticles by reducing the oxygen-containing functional groups and ultimately improve the EMI shielding ability of the core (CF)-shell (MXene) structure. The annealing was conducted at 350 °C under an inert atmosphere of continuous nitrogen flow for 6h in a tube furnace [55]. The obtained product was termed rMXene-CF (Fig. 1).

2.5. Preparation of CF/Epoxy resin composites by liquid composite molding

The core-shell CFRP composites were prepared by vacuum assisted resin infusion (VARI). The mold was first cleaned with alcohol, and then the layered CF fabric structure was built up step by step using a CF mat comprised of 6 CF layers to create the stacked preform. After that, a vacuum bag was utilized to seal the whole structure. A defoaming resin and curing agent compound with a 100:30weight ratio was introduced into the fabric under vacuum. Finally, the mold was moved into an oven to cure the resin at 90 °C for 8h.

2.6. Characterization

The topography of CF and MXene nanoparticles was studied by scanning electron microscopy (SEM, FEI Inspect-F). The surface morphology and thickness of the MXenes were measured by atomic force microscopy (AFM, Park XE7). The crystal structures of the MAX phase of Ti_3AlC_2 and the MXene $Ti_3C_2T_x$ nanoplatelets were studied by X-ray diffraction (XRD, Shimadzu-7000), while the chemical compositions of CF and MXenes were characterized by Fourier Transform Infrared (FTIR) spectroscopy. Raman spectroscopy data were collected using a Renishaw inVia confocal Raman Microscope in a backscattering configuration. The Raman signal was recorded from a 785 nm edge laser with a grating of 1200 grooves/min and at a laser power of 1 %. The surface chemical structure and functional group content were investigated by X-ray photoelectron spectroscopy (XPS). The wettability of carbon fibers was characterized *via* a dynamic contact angle analyzer (DCAT 21, Germany). Deionized water and glycerol were selected as solvents to calculate the polar portions, dispersion components and surface energy by using the Owens-Wendt method [56].

The three-point bending tests were performed according to the ASTM D790 standard, and the loading rate was 2 mm/min. Five specimens were tested for each set of samples. The electrical conductivity measurements were conducted using the four-probe method to remove the influence of the contact/conductor resistance [57]. Samples with a size of 22.86 × 10.16 mm were silver coated before the test to ensure better contact with the electrode. A Keithley multimeter was utilized to monitor the resistance changes and the related values was recorded in a LabView program.

The electromagnetic interference (EMI) shielding performance of the core-shell CFRP composites in the X-band (8.2–12.4 GHz) region was evaluated by a Vector Network Analyzer (VNA,CETC, AV3629D). The samples were rectangular (22.86 × 10.16 mm) and were fixed into the waveguide holder. Five specimens were prepared for testing and the final results were averaged from all the specimens. The main EMI shielding mechanism consisted of reflection (SE_R), absorption (SE_A), and multiple reflections (SE_M). The shielding effectiveness (SE_T) was calculated using Eq. (1). Generally, when the SE_A surpassed 15 dB, the SE_M could be neglected, and Eq. (2) is the one that is most commonly used [58,59]. The power coefficients of the reflection coefficient (R), transmission coefficient (T) and absorption coefficient (A) can be acquired by S parameters (S_{11}, S_{12}, S_{21}, S_{22}) according to Eq. (3), Eq. (4) and Eq. (5). Then the SE_R and SE_A can be calculated by the obtained power coefficients according to Eq. (6) and Eq. (7) [60].

$$SE_T(dB) = SE_R + SE_A + SE_M \quad (1)$$

$$SE_T(dB) = SE_R + SE_A \quad (2)$$

$$T = |S_{12}|^2 = |S_{21}|^2 \quad (3)$$

$$R = |S_{11}|^2 = |S_{22}|^2 \quad (4)$$

$$A = 1 - R - T \quad (5)$$

$$SE_R = -10\log(1 - R) \quad (6)$$

$$SE_A = -10\log\left(\frac{T}{1 - R}\right) \quad (7)$$

3. Results and discussion

3.1. Morphology and chemical composition of MXenes

The morphology transition from the dense multilayer state of the as-received MAX phase (Fig. 2a) to the loose accordion-like MXene phase presented in Fig. 2b proves that the etching and intercalation processes were successful. Fig. 2c presents the typical Tyndall effect of the MXene colloidal solution, which is further proof that the MXene nanosheets were well dispersed in the aqueous solution. The XRD results in Fig. 2d reveal that the (002) peak shifted from 9.48° for Ti_3AlC_2 to 6.62° for $Ti_3C_2T_x$, which indicates that the interlayer spacing increased from 0.468 nm to 0.668 nm, further confirming the successful intercalation process. The Raman spectra of $Ti_3C_2T_x$ and Ti_3AlC_2 are shown in Fig. 2e; the spectrum of $Ti_3C_2T_x$ displays two sharp peaks of A_{1g}(Ti, O, C) at 200 cm^{-1} and A_{1g}(C) around 725 cm^{-1}, which demonstrates the successful etching of Ti_3AlC_2 and the presence of the functional groups on the synthesized $Ti_3C_2T_x$ product [61]; The appearance of D band at 1360 cm^{-1} confirmed the presence of graphitic carbon on the $Ti_3C_2T_x$ and Ti_3AlC_2 surfaces [62]. The FTIR spectrum of the synthesized MXene is presented in Fig. 2f. The typical peaks at 589 cm^{-1} and 3430 cm^{-1} correspond to the stretching vibration of Ti–O bonds and the hydrogen-bonded –OH, which confirms that Al atoms were replaced by –OH functional groups [63].The results from the XPS analysis of MXene nanoplatelets are illustrated in Fig. 2g-i; the Ti and O elements appeared in the survey spectrum while the corresponding Ti–O and C–OH fitting peaks that are present in the Ti_{1s} and O_{1s} spectra fully confirm the existence of –OH and –O functional groups, endowing MXene nanoparticles with hydrophilic properties, in agreement with previous literature reports [64,65].

3.2. Surface morphology of CF

SEM was utilized to evaluate the surface morphology of the core-shell MXene-CF structures after the EPD process and the thermal annealing treatment. As shown in Fig. 3a and e, the pretreated CF presented a relatively smooth surface morphology and many grooves can be observed, indicating that the desizing process successfully removed the sizing agents from the CF. Fig. 3b and f reveal a typical core-shell structure. The CF can be considered as the core, while the flower-shaped MXene shell was self-assembled during the EPD process due to electrostatic effects. The CF are highly electronegative as they possess abundant oxygen-containing functional groups such as hydroxy and carboxyl. On the contrary, the MXene nanoparticles display electropositive properties after mixing with magnesium chloride hexahydrate. Thus, a self-assembly behavior can be observed during the EPD process. The electric field applied during the EPD process facilitates the electrostatic assembly. Consequently, the flower-like MXene shell was successfully and homogeneously deposited on the surface of the inner CF core as can be realized from the SEM images. The EDS elemental maps of

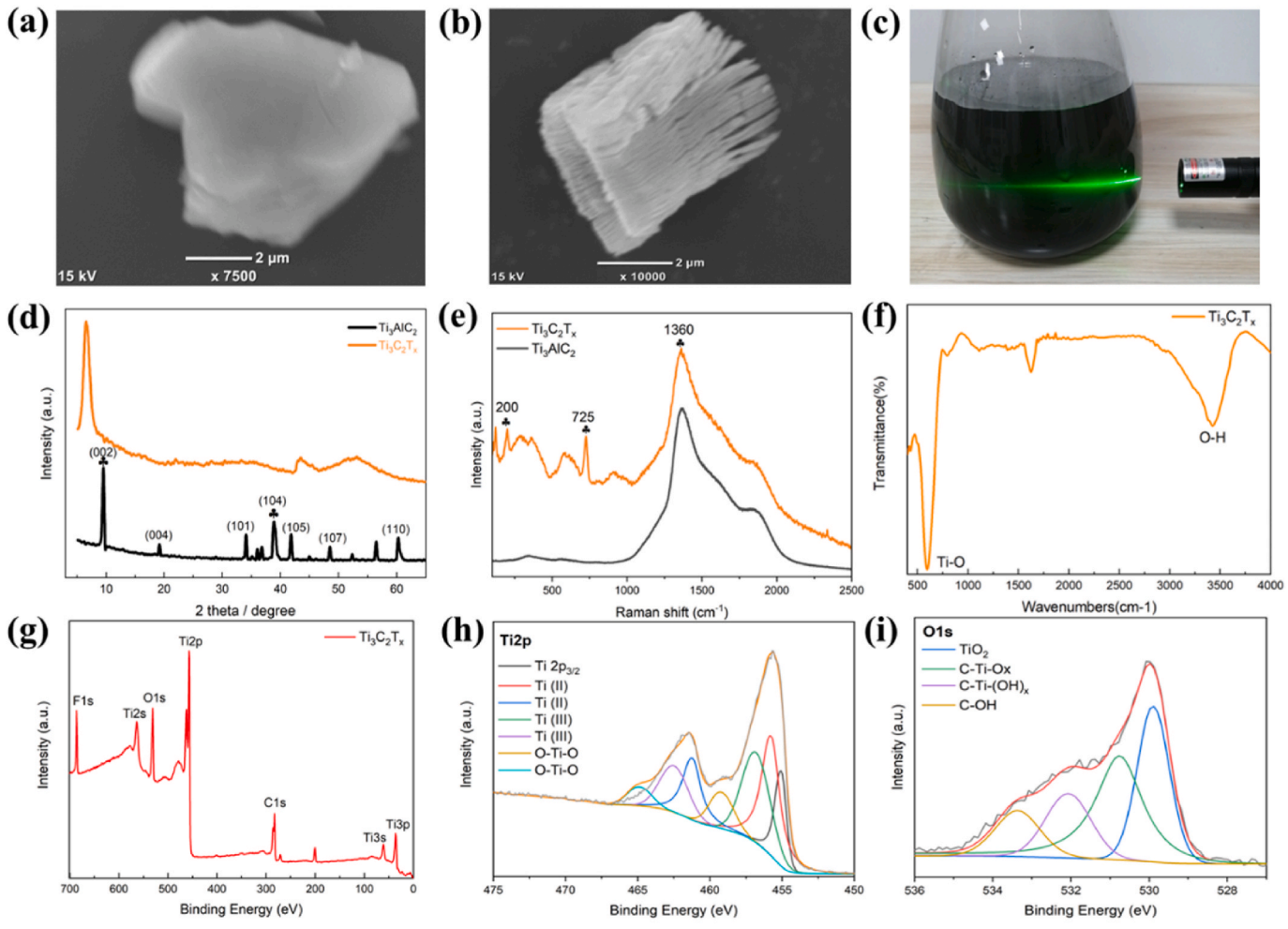

Fig. 2. SEM images of (a) Ti_3AlC_2, (b) $Ti_3C_2T_x$; (c) Tyndall effect of 0.125 mg/mL $Ti_3C_2T_x$ in a water suspension; (d) XRD patterns comparison between Ti_3AlC_2 and $Ti_3C_2T_x$; (e) FTIR spectrum of $Ti_3C_2T_x$; (f) Raman spectroscopy of $Ti_3C_2T_x$; XPS spectra of $Ti_3C_2T_x$ (g) survey scan, (h) Ti2p spectrum, (i) O1s spectrum.

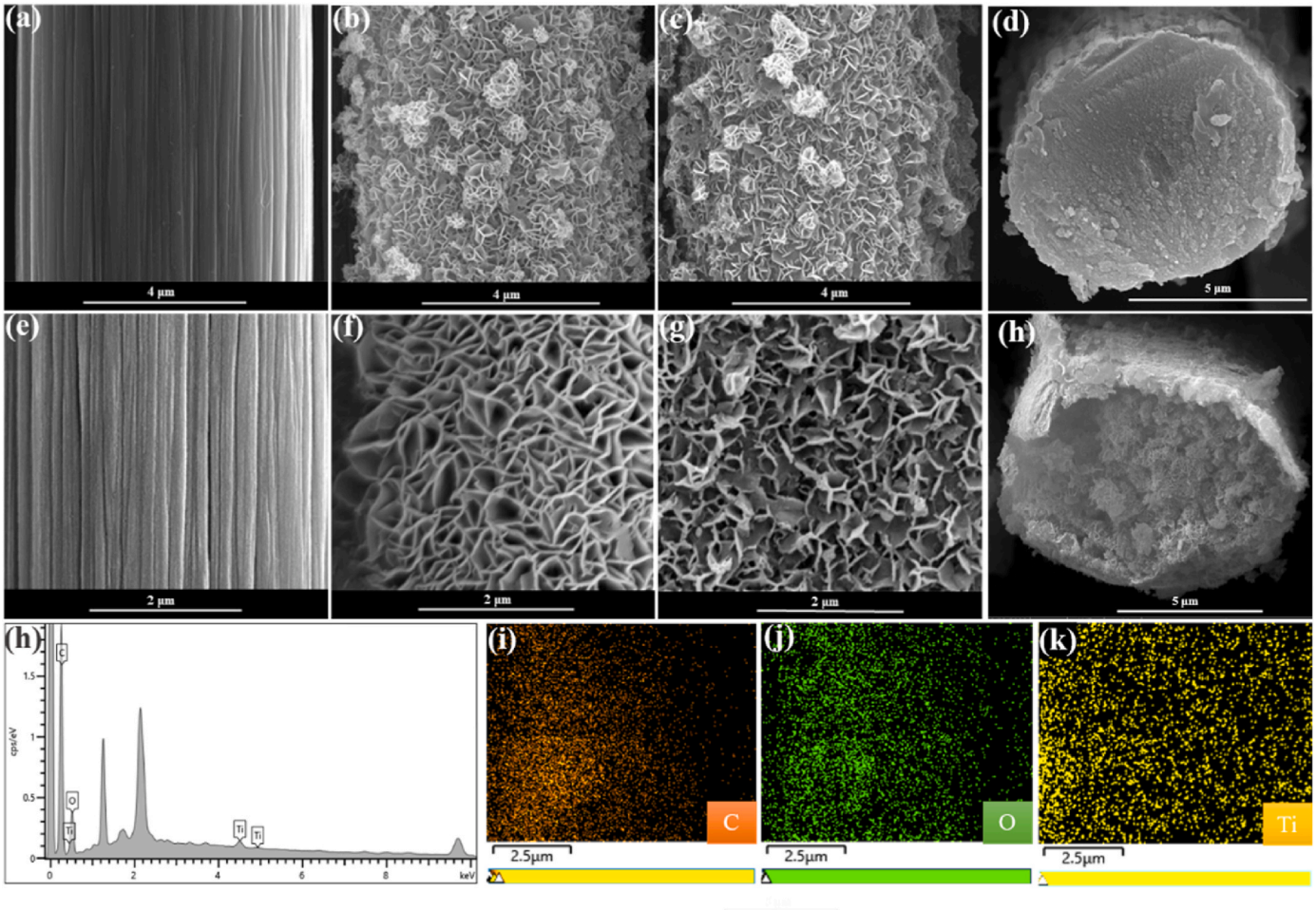

Fig. 3. SEM morphologies of (a) CF, (b) MXene-CF, and (c) rMXene-CF. Figures (e)–(g) are magnified images of (a)–(c). Figures (d) and (h) are the cross-sections of Fig.(a) and Fig.(b). Figures (h)–(k) show the EDS mapping results of MXene-coated CF.

the MXene coated fibers collected from the SEM and presented in Fig. 3h-k also reveal the homogenous distribution of the Ti, C, O elements on the surface of CFs.

3.3. Raman analysis of CF

Raman spectra were collected from the MXene-deposited nanoparticles onto the CF fabric. As shown in Fig. 4, two broad peaks were observed in all three CF fabrics. The peak observed at 1330-1350 cm^{-1} is related to the D band, which indicates disordered carbon and/or crystal defects present in the CF structure, while the peak observed at 1580-1600 cm^{-1} corresponds to the G band, representing the graphitic lattice [66]. As a result, the intensity ratio of the D band to G band (I_D/I_G) can be used as an indication of the amount of structural defects [67]. In comparison with the spectrum of the MXene shown in Fig. 4 the newly-appeared characteristic peaks located at 200 cm^{-1} and 725 cm^{-1} at the MXene-CF and rMXene-CF spectra are evidence that the MXene nanoparticles were successfully deposited onto the surface of the CF fabrics [61]. It is noteworthy that the I_D/I_G ratio fluctuated, increasing from 1.09 to 1.4 for neat CF and the MXene-CF samples respectively, and then decreasing to 1.11 for the rMXene-CF sample. During the EPD process, the positively-charged MXene nanoparticles self-assembly onto the negatively-charged CF surface under the electric field and due to the electrostatic adsorption effect. As a consequence, the increased I_D/I_G ratio corresponds to the increased defects as a result of hydrogen bonding between the MXene nanoparticles and the CF [67]. However, after the thermal annealing process, the defect content of the rMXene-CF

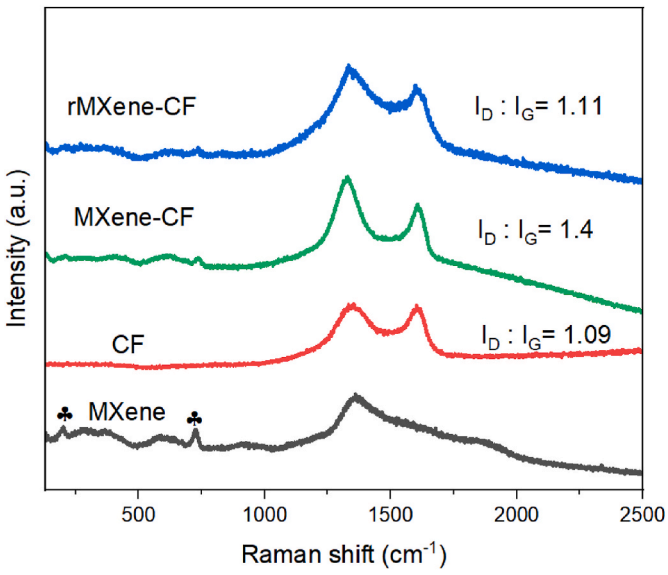

Fig. 4. Raman spectra of the MXene, CF, MXene-CF, and rMXene-CF samples.

structure decreased, due to the subsequent destruction of the hydrogen bonds and the removal of the oxygen-containing groups. Likewise, the observed trend of an initial increase followed by a decrease in the I_D/I_G

ratio, from CF to MXene-CF and rMXene-CF aligns well with the C:O ratio in the XPS analysis and the surface energy values obtained from the contact angle tests, as detailed in Section 3 and Section 6 of the Supporting Information.

3.4. Mechanical properties of CF/EP composites

3.4.1. Flexural properties

The three-point bending method was employed to assess the flexural properties of the CFRPs (Fig. 5a). The stress-strain curves are presented in Fig. 5b and as can be seen from Fig. 5c, a 26 % enhancement of flexural strength was recorded; the untreated CF/EP composite displayed a strength of 511.3 ± 21.7 MPa that increased to 642.4 ± 15.2 MPa after the introduction of the MXene nanoparticles. However, the subsequent thermal annealing treatment seems to reduce the flexural performance of the MXene-CFRP composites, by reducing the bending strength to 569.6 ± 14.9 MPa. A comparison of flexural strength improvement as a function of the suspension concentration between this work and other EPD-based modification methods is presented in Fig. 5f and Table 1 and further demonstrates the superiority of both the proposed EPD process and the produced core-shell MXene/CF structure, towards improvement of the mechanical properties of nanoparticle-modified CFRPs.

3.4.2. Mechanical strengthening mechanism

The SEM images of the fractured surfaces as well as the possible mechanical strengthening mechanism was illustrated in Fig. 6. The failure of the untreated CF/EP composite takes place *via* debonding of the CF from the matrix, leading to brittle failure. On the contrary, the fracture mechanism transforms to ductile in the case of the MXene-CF/EP composites. The simultaneous failure of the CF and the epoxy matrix took place thanks to the effective stress transfer from the epoxy to the CF as a result of the presence of the MXene nanoparticles at the interface of the two materials. The oxygen-containing functional groups (e.g., hydroxyl groups) interacted with similar carboxyl and hydroxy ones on the CF surface to construct hydrogen bonds as can be realized from the respective FTIR spectra presented in Fig. S1 of the Supporting Information. The mechanical interlocking effect can also be regarded as another crucial factor; the stiff MXene nanoparticles (a single layer of $Ti_3C_2T_x$ displays a Young's modulus of 0.33 ± 0.03 TPa [68]) inserted into the resin inhibited the propagation of the cracks. Consequently, more energy was needed to pull the nanoparticles out from the interface or fracture them. The conducted fractography analysis (Fig. 6a–c) further revealed the above-mentioned failure mechanisms. Compared to the smoother fracture surface of the CF/EP composites corresponding to the weak fiber/matrix interface shown in Fig. 6a and d, the micrograph

Table 1
Literature comparison of CFRP flexural strength improvement, where the CFs were coated by nanoparticles *via* electrophoretic deposition.

Polymer	Fillers	EPD conditions	Suspension Concentration (mg/mL)	Flexural strength Improvement (%)	Ref
EP	G-OH/CF	5A, 30min	1	5.1	[69]
EP	G-COOH/CF	5A, 30min	1	9.6	[69]
EP	GO/CF	5A, 30min	1	6	[69]
EP	CNF/CF	5A, 30min	0.5	4.2	[70]
EP	Graphene/CF	5A, 30min	0.5	6.5	[70]
EP	CNT/CF	5A, 30min	0.5	9	[70]
EP	CNT-COOH	5A, 30min	1	10	[71]
EP	CNT-OH	5A, 30min	1	3	[71]
EP	O-CNTs/CF	24V, 5min	0.3	9.46	[72]
Vinyl ester resin	CNT/CF	5A, 30min	0.5	10.3	[73]
Vinyl ester resin	CNT-COOH/CF	5A, 30min	0.5	13.8	[73]
EP	GO/CF	1V, 30min	0.5	14	[74]
EP	MXene-CF	20V, 30min	0.125	25.7	This work
EP	rMXene-CF	20V, 30min	0.125	11.4	This work

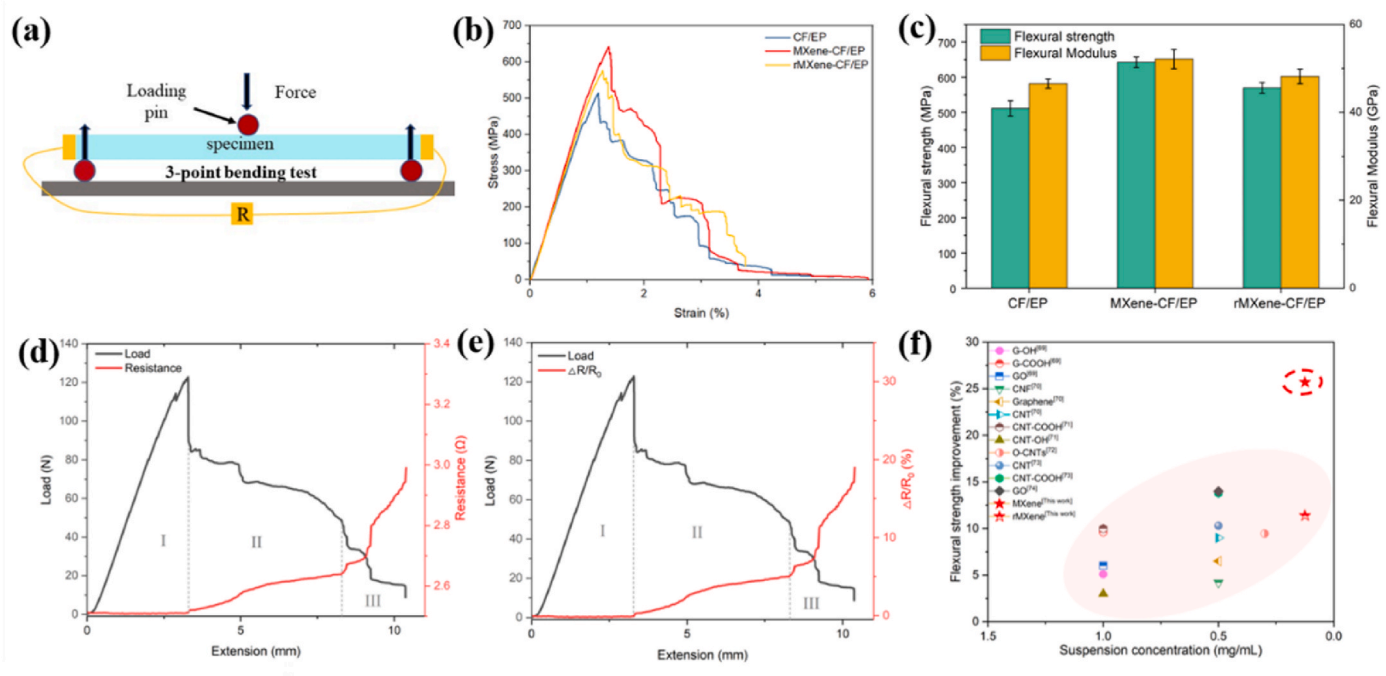

Fig. 5. (a) The test setup, (b) stress strain curves and (c) results on the flexural properties of the CF/EP, MXene-CF/EP, and rMXene-CF/EP composites, respectively; (d–e) mechanical-electrical response of MXene-CF/EP composites; (f) comparison of flexural strength improvement between our works and related literature.

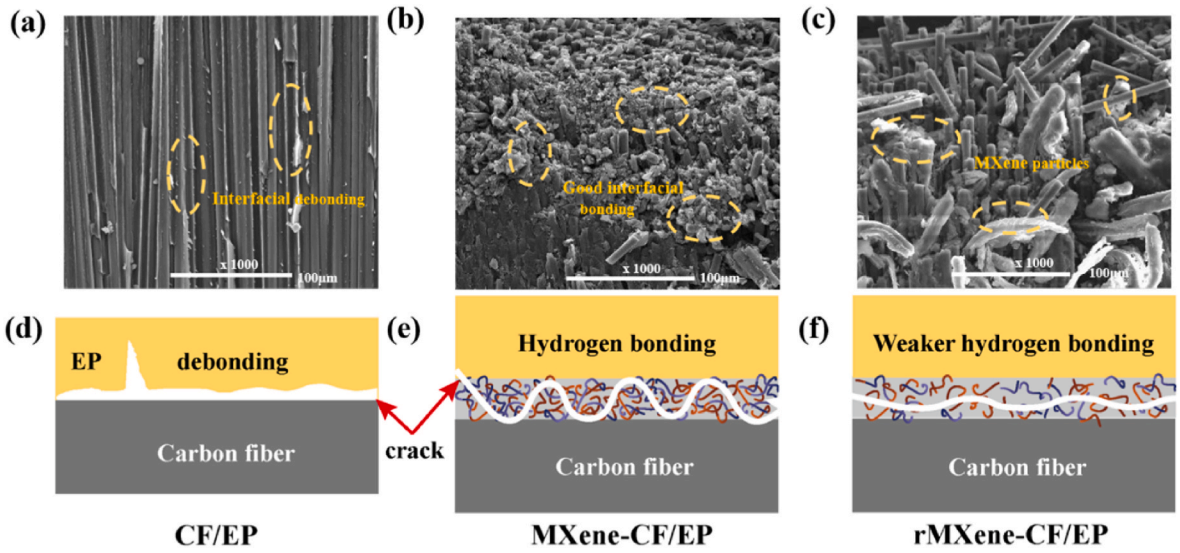

Fig. 6. The SEM morphologies (a–c) characterizations and corresponding interface failure and matrix cracking propagations (d–f) of the CF/EP, MXene-CF/EP, and rMXene-CF/EP composites.

of the MXene-CF/EP composites in Fig. 6b presented a considerable amount of debris from the epoxy matrix which is indication of higher force needed to induce fracture and improved interfacial strength under the effect of hydrogen bonding between CF and MXene (Fig. 6e). A similar observation can be made for the rMXene-CF/EP composites in Fig. 6c, with some pronounced matrix cracks; however, a larger amount of rMXene agglomerates were witnessed, which may be ascribed to the thermal de-functionalization effect that induced shrinkage and possible detachment from the CF surface [50]. These observations are in good agreement with the corresponding flexural properties since the reduction in the flexural strength and modulus after thermal annealing could be ascribed to the decomposition of the oxygen-containing groups at elevated temperatures and the subsequent destruction of hydrogen bonding (Fig. 6f) as well as weakening of the interface.

3.4.3. *In-situ damage sensing*

In-situ damage sensing was employed to detect the initiation and propagation of cracks during loading. The three-stage load-displacement-resistance curves of the MXene-CFRP composite are shown in Fig. 5d. The first stage corresponds to the elastic deformation area, where the crack was stationary and the load increased linearly. The resistance remained constant at this stage as no significant damage happened. A sudden drop of load can be observed at the second stage, denoting the initiation of matrix cracks and the propagation of cracks to the MXene-coated fibers. At this stage the phenomena of fiber-matrix debonding, nanoparticle pull-out, alongside possible fiber fracture starts to take place. Accordingly, the resistance increased unevenly due to the uneven separation of the upper and lower laminates [35]. The last stage displays a rapid decrease of load as a consequence of acute crack growth and delamination until failure. As a result, the resistance increases pronouncedly. The resistance change over the relative intrinsic resistance change ($\Delta R/R_0$) was also studied (Fig. 5e), and the results displayed excellent coherence both in terms of time of damage occurrence and electrical signal differences. As soon as the matrix cracks, the fiber break and debonding takes place, the corresponding voltage alterations are able to be detected simultaneously and with high accuracy due to the breakdown of the MXene-CF conductive path. Interestingly, the corresponding curves of the pristine CFRP composites shown in Fig. S5 indicate that the MXene-CFRP composites witnessed smaller resistance-change (around 18 % difference) than the CFRP composites (nearly 60 % difference). Such a result can be attributed to fractured MXene nanoparticles that were able to form new conductive paths during the tests to retain a relatively small resistance variation ($\Delta R/R_0$). This is in agreement with the electrical conductivity measurements reported in the next section, since improvement of conductivity was observed in both the in-plane and out-of-plane directions after the introduction of the MXenes into the CFRP composites. As a result, the MXene-CFRP composites clearly display the potential for highly accurate in-situ damage inspection and structural health monitoring.

The possible mechanism behind the damage sensing capability was analyzed and illustrated in Fig. 7.

It is well known that CFRP composites display weak out-of-plane performance, as the insulated resin between CF layers not only hinders the transmission of electric signals but shows inferior mechanical properties. Hence, the electrical conductivity of CFRP composites in the through-thickness direction depends on the direct contact between the adjacent CF layer. As shown in Fig. 7a and c, there can be areas within the unmodified CFRPs where adjacent CF layers aren't directly connected but they are separated by insulating gaps. In this case, the conductive path in the thickness direction was interrupted and resulted in the weak conductive performance in the out-of-plane direction, corresponding to the results shown in Fig. 8. For the case of the MXene-CFRP composites, the highly conductive MXene nanoparticles offer an opportunity to improve the out-of-plane conductivity of the CFRPs. As presented in Fig. 6d, the vertically aligned MXene nanoparticles bridged the insulating gaps and constructed a highly effective conductive path between layers, which effectively limits the dependence of unmodified CFRP composites on the physical contacts for the optimization of the stability of the sensing signal [36]. As a result of the EPD process, the MXene nanoparticles were uniformly deposited onto the CF surface and ensured a good linkage *via* electrostatic adherence and hydrogen-bonding effects [75].

3.5. *Electrical conductivity of CFRPs*

The four-probe method was utilized to evaluate the electrical conductivity of the modified CFRP composites (details on the measurement process are presented in Section 4 of Supporting Information). The pristine CF/EP composite presented low electrical conductivity values due to the non-conductive nature of the epoxy resin. The obvious differences in the electrical conductivity results both in the through-plane and in-plane directions are the direct result of the anisotropic electrical properties of CF [76]. The electrical conductivity of the CF/EP sample in the through-thickness direction was 38.9 S/m, while the corresponding

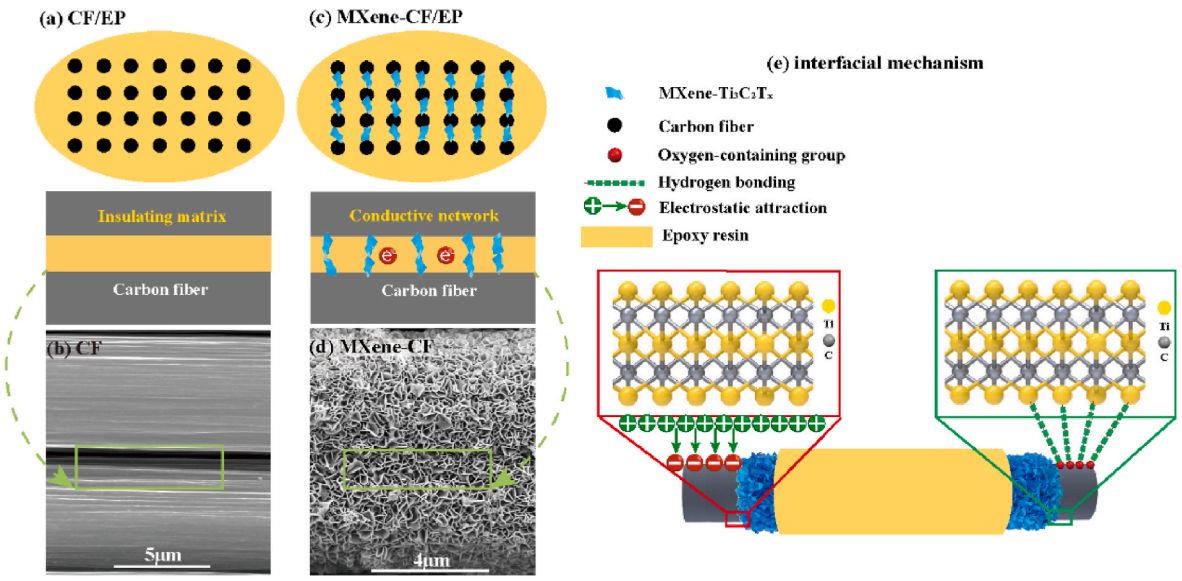

Fig. 7. Schematic diagram of electromechanical-response process for the pristine CFRP composites (a–b) and the MXene-CFRP composites (c–d) as well as their corresponding interfacial mechanisms (e).

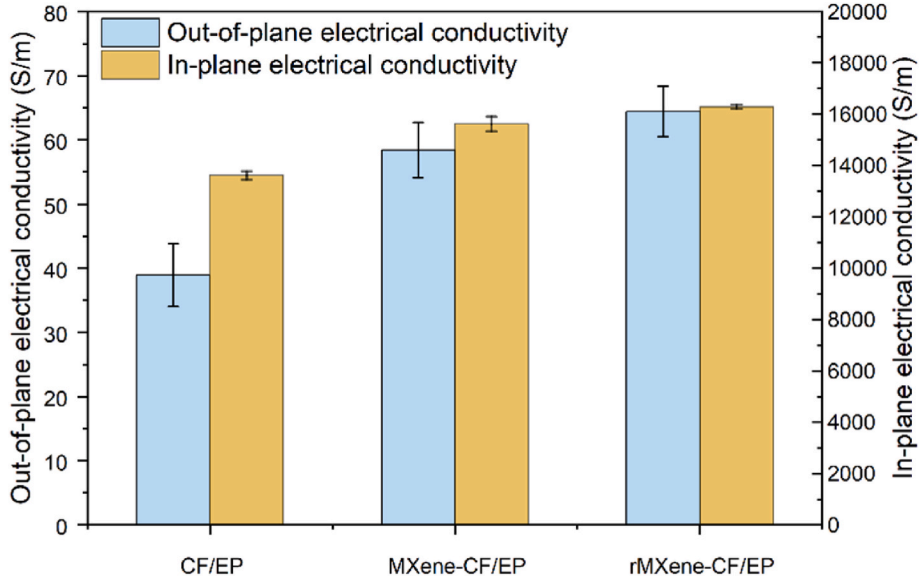

Fig. 8. The out-of-plane/in-plane electrical conductivities of the CF/EP, MXene-CF/EP, and rMXene-CF/EP composites.

value in the in-plane direction reached 13615.5 S/m (Fig. 8). After the EPD of MXene nanoparticles onto the CF, the electrical conductivity in the through-thickness and in-plane directions increased to 58.4 S/m and 15624.3 S/m, respectively. Such a phenomenon can be ascribed to the dual-conductive network formed by the uniformly distributed, highly-conductive MXene nanoparticles and the CF-based skeleton, which contributed to the optimization of the conductivity of the structure. The thermal annealing treatment enabled a reduction of the oxygen-containing functional groups and an improvement of the electrical conductivity of MXene nanoparticles; the rMXene-CF/EP composite displayed an electrical conductivity of 64.44 S/m in the through-thickness direction and of 16292 S/m in the in-plane direction. In conclusion, the introduction of MXene nanoparticles onto the surface of the CF can be beneficial in ameliorating the electrical performance of the CFRPs *via* the construction of a dual-conductive network, while the thermal annealing effect can further optimize the conductivity of the core-shell MXene-CF structure. The overall increases correspond to an improvement of 66 % in the out-of-plane electrical conductivity and an enhancement of 20 % in the in-plane electrical conductivity.

3.6. EMI shielding performance of CFRPs

The EMI SE was characterized using the wavelength guide method. As shown in Fig. 9 (a) and (b), the neat CF/EP composite samples displayed a 28.7 dB EMI shielding effectiveness. Once the MXene nanoparticles were deposited onto the CF, the EMI SE of the MXene-CF/EP composites was improved to a value of 32.9 dB at 12.4 GHz. Ultimately, this value was further enhanced to 34.4 dB (a 20 % improvement compared to the pristine CFRP composite) after thermal annealing (rMXene-CF/EP). The corresponding absorption effectiveness (SE_A) and reflection values (SE_R) were 24.6 dB and 9.8 dB, respectively. The coefficient A (that represents the ability of the shielding materials to absorb radiation) displayed a low value of 0.1 while the value of coefficient R (that represents the ability of the shielding materials to reflect

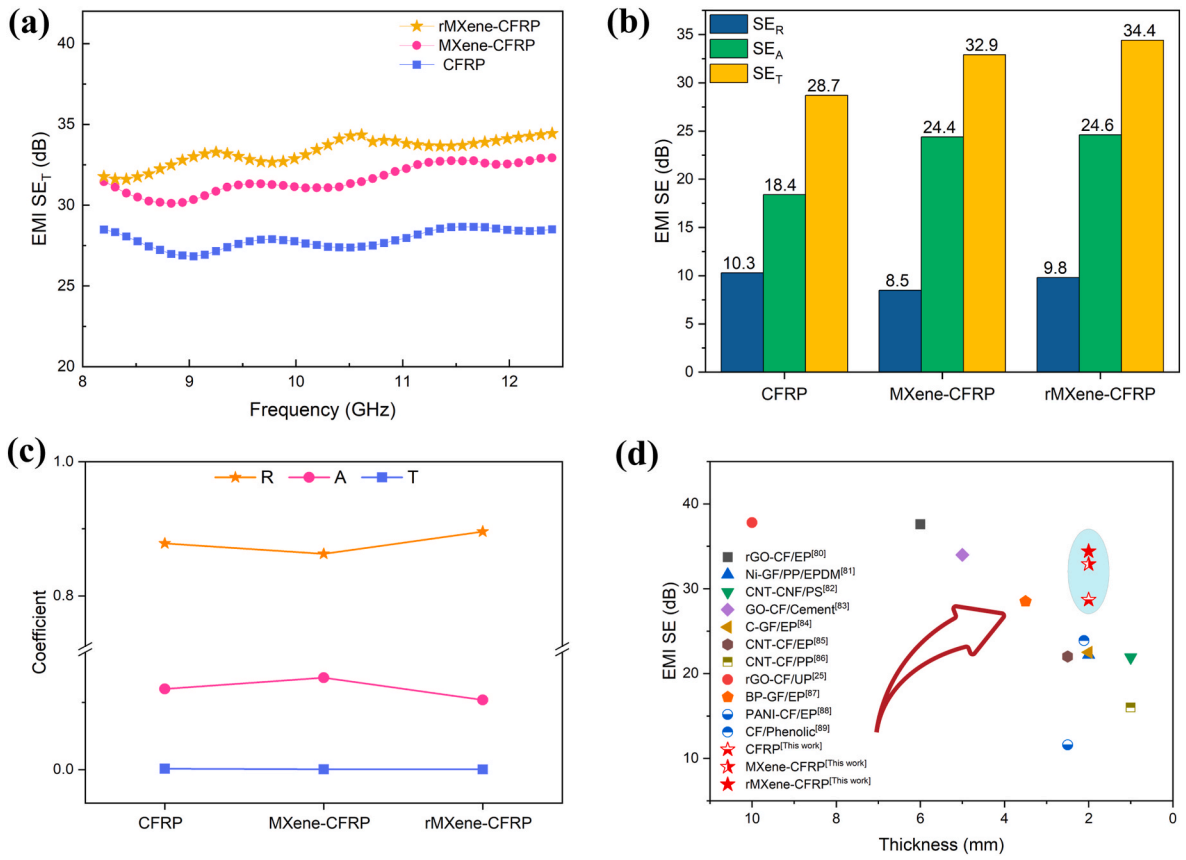

Fig. 9. (a) EMI shielding effectiveness transmission (SE_T) curves; (b) collective EMI SE results (the results are average from 5 measurements); (c) The corresponding reflection (R), absorption (A), and transmission (T) values in the X-band; (d) Comparison of EMI shielding performance as a function of thickness with data from literature.

radiation) was high, of the order of 0.9 (Fig. 9c); revealing that the dominant EMI shielding mechanism was reflection, which can be ascribed to the conductivity of carbon fibers. As shown in Fig. 9d and Table 2, compared with other literature values of the EMI SE of fiber reinforced composites as a function of the thickness of the structure, the materials reported herein, outperform the current state-of-the-art and display SE comparable with structures almost 3 times thicker.

Table 2
Comparison of the shielding effectiveness (SE) of polymer composites and nanocomposites from the literature.

Matrix	Filler	Measurement method	Thickness (mm)	SE (dB)	Ref
EP	rGO-CF	waveguide	6	37.6	[80]
PP/ EPDM	Ni-GF	waveguide	2	22.2	[81]
PS	CNT-CNF	waveguide	1	21.9	[82]
Cement	GO-CF	waveguide	5	34	[83]
EP	C-GF	waveguide	2	22.5	[84]
EP	CNT-CF	waveguide	2.5	22	[85]
PP	CNT-CF	coaxial transmission	1	16	[86]
UP	rGO-CF	waveguide	10	37.8	[25]
EP	BP-GF	waveguide	3.5	28.5	[87]
EP	PANI-CF	coaxial transmission	2.5	11.6	[88]
Phenolic	CF	waveguide	2.11	23.9	[89]
EP	CF	waveguide	2	28.7	This work
EP	MXene-CF	waveguide	2	32.9	This work
EP	rMXene-CF	waveguide	2	34.4	This work

3.7. EMI shielding mechanism of MXene-modified CFRPs

The proposed EMI shielding mechanism is illustrated in Fig. 10. As soon as the incident waves arrive at the CF surface, some of them are reflected because of the impedance mismatch between the air and the fiber. The remaining waves enter the laminate and are subsequently multi-reflected and scattered among different layers due to the "high depth" that the laminate possesses as a result of the layer-by-layer assembly [77]. The internal scattering further extends the EM propagation path length and provides more opportunities for interaction between the EM radiation and the shield, leading to an increased attenuation by absorption [13]. After the EPD process, the uniformly deposited MXene nanoparticles increased the specific surface area and interface area of the CF, which consequently accelerated the attenuation of the electromagnetic wave. Meanwhile, the MXene skeleton acts as a secondary EMI shielding layer and is introduced into the 3D CF fabric structure to construct a more completed dual carbon-containing 3D framework (Fig. 9a upper left) [20]. The MXene/CF hierarchical structure contains more abundant free electrons and is able to form a highly-efficient conductive network [60], which is beneficial for the production of considerable electromagnetic field-induced current or heat and to further intensify the conduction loss effect [78]. Multiple heterointerface polarization also takes place as a result of the CF/MXene/EP core-shell microstructures that dissipate the electromagnetic waves by dielectric loss and the abundant surface functional groups (Fig. 8b upper right). It is well known that dielectric loss is one main dissipation forms of the incident magnetic microwaves, which consists of dipole polarization and interfacial polarization. The dipole polarization phenomenon usually happens in the areas where the functional groups, defects and dangling bonds of MXene nanoparticles are located. Therefore, stacking

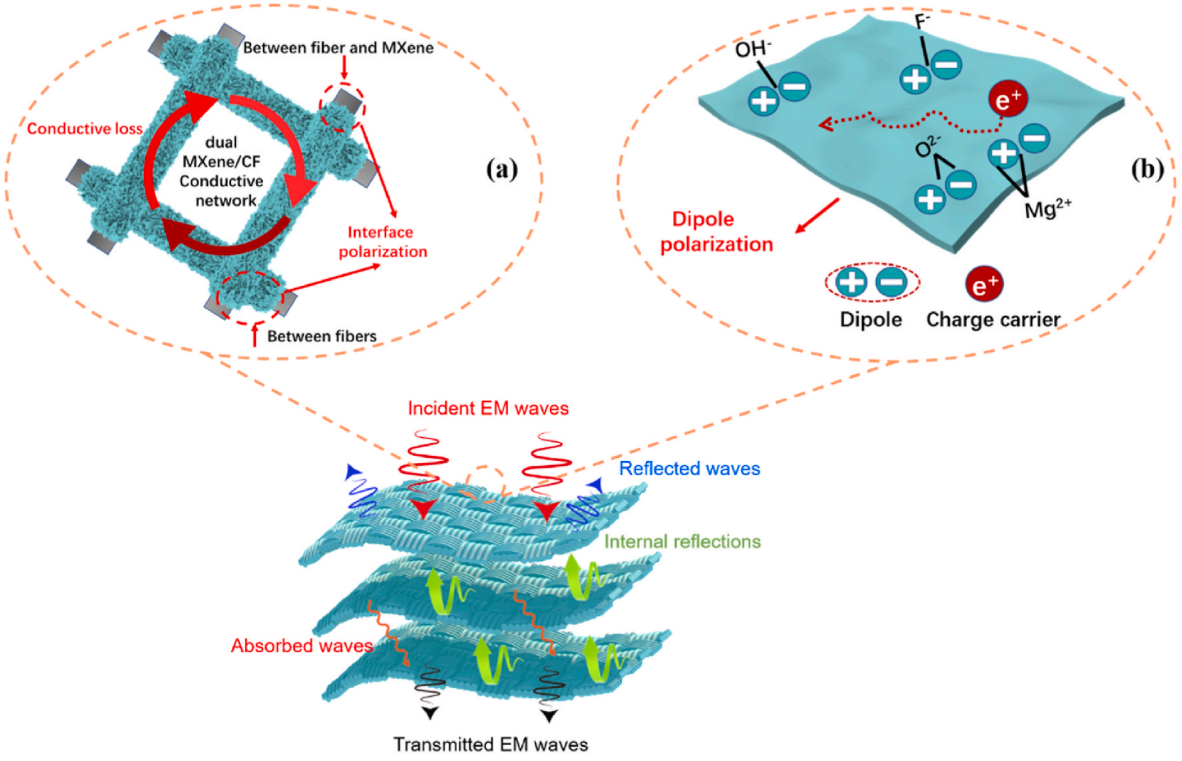

Fig. 10. Schematic of EMI shielding mechanism of the MXene modified CFRP composites. (a) Conductive loss effect thanks to the formation of the dual MXene/CF conductive network; (b) Dialectic loss mechanism due to the dipole polarization effect on MXene and CF surfaces.

defects on the surface of MXene would enhance the EM wave absorption effect *via* dipole polarization losses [13,79]. In conclusion, the high EMI SE was ascribed to multiscale EM energy consumption mechanisms from the MXene/CF hierarchical microstructure, including polarization from multiple inhomogeneous interfaces, the conductive loss effect and the possibly dipole polarization.It is important to point out that after the thermal annealing process, the conductive loss can be more pronounced due to the enhanced electrical conductivity of the rMXene/CFRP composite by removing the oxygen-containing groups. Finally, the defects also contribute to the dipole polarization loss [25].

4. Conclusion

A set of highly-conductive and mechanically robust MXene@CF core-shell composites were fabricated *via* EPD process in this present work. A homogeneous deposition of the MXene nanoparticles was achieved on the CF surfaces by electrochemical engineering. MXene nanoparticles work effectively towards the creation of a robust and conductive interface, where the synergistic effect of mechanical interlocking and hydrogen bonding significantly strengthen the attachment between the CF and the resin. Consequently, the constructed hierarchical composite structure (MXene-CF/EP) displayed exceptional mechanical properties as well as superior in-situ damage sensing ability, while the removal of the oxygen-containing groups through thermal annealing (rMXene-CF/EP) led to superior conductive properties both in-plane and through-plane and exceptional EMI shielding performance. The flexural strength, out-of-plane electrical conductivity, and EMI SE increased by 26 %, 66 %, and 20 %, respectively. This work proposed an attractive EPD strategy for effectively manufacturing mechanically robust MXene/CFRP composite and provided valuable insights into developing EMI shielding materials.

CRediT author statement

Yi Hu: Investigation, Visualization, Methodology, Data curation, Writing- Original draft preparation. Guoyu Wang: Visualization, Investigation, Junzhen Chen: Visualization, Investigation. Yujun Li: Investigation, Ming Dong: Investigation, Han Zhang: Writing- Reviewing and Editing, Emiliano Bilotti: Writing- Reviewing and Editing, Jianjun Jiang: Conceptualization, Methodology, Supervision, Funding Acquisition, Writing- Reviewing and Editing. Dimitrios G. Papageorgiou: Conceptualization, Supervision, Funding Acquisition, Writing- Original draft preparation, Writing- Reviewing and Editing.

Declaration of competing interest

The authors declare that they have no known competing financial interests or personal relationships that could have appeared to influence the work reported in this paper.

Data availability

Data will be made available on request.

Acknowledgements

This research is supported by the Key Research and Development Projects of Shaanxi Province, China (grant no. 2020ZDGY01-01), the Fundamental Research Funds for the Central Universities, China (grant no. D5000220202), and the National Natural Science Foundation of China (grant no. 51573148). D.G.P., E.B. and H.Z. acknowledge the support from “Graphene Core 3” GA: 881603 which is implemented under the EU-Horizon 2020 Research & Innovation Actions (RIA) and is financially supported by EC-financed parts of the Graphene Flagship.

Appendix A. Supplementary data

Supplementary data to this article can be found online at https://doi.org/10.1016/j.compscitech.2023.110356.

References

[1] G.M. Weng, J.Y. Li, M. Alhabeb, C. Karpovich, H. Wang, J. Lipton, K. Maleski, J. Kong, E. Shaulsky, M. Elimelech, Y. Gogotsi, A.D. Taylor, Layer-by-Layer assembly of cross-functional semi-transparent MXene-carbon nanotubes composite films for next-generation electromagnetic interference shielding, Adv. Funct. Mater. 28 (44) (2018).

[2] J. Hong, P. Xu, H. Xia, Z.Z. Xu, Q.Q. Ni, Electromagnetic interference shielding anisotropy enhanced by CFRP laminated structures, Compos. Sci. Technol. 203 (2021).

[3] H.X. Zhu, K.K. Fu, B. Yang, Y. Li, Nickel-coated nylon sandwich film for combination of lightning strike protection and electromagnetic interference shielding of CFRP composite, Compos. Sci. Technol. 207 (2021).

[4] C. Xie, Y. Fang, Y. Chen, J. Liu, Z.-X. Guo, X. Hao, C. Li, X. Tuo, Aramid-based highly conductive composite films by incorporating graphene for electromagnetic interference shielding and Joule heating applications, Compos. Sci. Technol. 236 (2023), 109992.

[5] N. Yousefi, X.Y. Sun, X.Y. Lin, X. Shen, J.J. Jia, B. Zhang, B.Z. Tang, M.S. Chan, J. K. Kim, Highly aligned graphene/polymer nanocomposites with excellent dielectric properties for high-performance electromagnetic interference shielding, Adv. Mater. 26 (31) (2014) 5480–5487.

[6] J.J. Huang, D. Sun, G. Li, X.K. Wang, H.D. Ma, W.Q. Zhang, Z.M. Chen, H.L. Li, C. M. Gui, Lightweight and textured Ni@Cu-encapsulated carbon tube with outstanding electromagnetic interference shielding performance, Compos. Sci. Technol. 228 (2022).

[7] M. Wang, X.-H. Tang, J.-H. Cai, H. Wu, J.-B. Shen, S.-Y. Guo, Construction, mechanism and prospective of conductive polymer composites with multiple interfaces for electromagnetic interference shielding: a review, Carbon 177 (2021) 377–402.

[8] F. Safdar, M. Ashraf, A. Javid, K. Iqbal, Polymeric textile-based electromagnetic interference shielding materials, their synthesis, mechanism and applications - a review, J. Ind. Textil. 51(5)(2021) 7293S-7358S.

[9] B.G. Soares, G.M.O. Barra, T. Indrusiak, Conducting polymeric composites based on intrinsically conducting polymers as electromagnetic interference shielding/microwave absorbing materials-A review, Journal of Composites Science 5 (7) (2021).

[10] H.T. Zhang, Y. Guo, X. Zhang, X.Q. Wang, H. Wang, C.S. Shi, F. He, Enhanced shielding performance of layered carbon fiber composites filled with carbonyl iron and carbon nanotubes in the koch curve fractal method, Molecules 25 (4) (2020).

[11] Z.Z. Guo, P.G. Ren, J. Wang, J.H. Tang, F.D. Zhang, Z. Zong, Z.Y. Chen, Y.L. Jin, F. Ren, Multifunctional sandwich-structured magnetic-electric composite films with Joule heating capacities toward absorption-dominant electromagnetic interference shielding, Compos. B Eng. 236 (2022).

[12] N.N. Wu, Q. Hu, R.B. Wei, X.M. Mai, N. Naik, D. Pan, Z.H. Guo, Z.J. Shi, Review on the electromagnetic interference shielding properties of carbon based materials and their novel composites: recent progress, challenges and prospects, Carbon 176 (2021) 88–105.

[13] A. Iqbal, P. Sambyal, C.M. Koo, 2D MXenes for electromagnetic shielding: a review, Adv. Funct. Mater. 30 (47) (2020).

[14] S.K. Singh, M.J. Akhtar, K.K. Kar, Hierarchical carbon nanotube-coated carbon fiber: ultra lightweight, thin, and highly efficient microwave absorber, ACS Appl. Mater. Interfaces 10 (29) (2018) 24816–24828.

[15] S.T. Hsiao, C.C.M. Ma, H.W. Tien, W.H. Liao, Y.S. Wang, S.M. Li, Y.C. Huang, Using a non-covalent modification to prepare a high electromagnetic interference shielding performance graphene nanosheet/water-borne polyurethane composite, Carbon 60 (2013) 57–66.

[16] M.H. Al-Saleh, Influence of conductive network structure on the EMI shielding and electrical percolation of carbon nanotube/polymer nanocomposites, Synth. Met. 205 (2015) 78–84.

[17] S. Ayub, B.H. Guan, F. Ahmad, M.F. Javed, A. Mosavi, I. Felde, Preparation methods for graphene metal and polymer based composites for EMI shielding materials: state of the art review of the conventional and machine learning methods, Metals 11 (8) (2021).

[18] Z. Lei, D. Tian, X. Liu, J. Wei, K. Rajavel, T. Zhao, Y. Hu, P. Zhu, R. Sun, C.P. Wong, Electrically conductive gradient structure design of thermoplastic polyurethane composite foams for efficient electromagnetic interference shielding and ultra-low microwave reflectivity, Chem. Eng. J. 424 (2021).

[19] C.-B. Li, Y.-J. Li, Q. Zhao, Y. Luo, G.-Y. Yang, Y. Hu, J.-J. Jiang, Electromagnetic interference shielding of graphene aerogel with layered microstructure fabricated via mechanical compression, ACS Appl. Mater. Interfaces 12 (27) (2020) 30686–30694.

[20] X.M. Bian, L. Liu, H.B. Li, C.Y. Wang, Q. Xie, Q.L. Zhao, S. Bi, Z.L. Hou, Construction of three-dimensional graphene interfaces into carbon fiber textiles for increasing deposition of nickel nanoparticles: flexible hierarchical magnetic textile composites for strong electromagnetic shielding, Nanotechnology 28 (4) (2017).

[21] S. Gupta, N.H. Tai, Carbon materials and their composites for electromagnetic interference shielding effectiveness in X-band, Carbon 152 (2019) 159–187.

[22] Y. Yuan, W.L. Yin, M.L. Yang, F. Xu, X. Zhao, J.J. Li, Q.Y. Peng, X.D. He, S.Y. Du, Y. B. Li, Lightweight, flexible and strong core-shell non-woven fabrics covered by reduced graphene oxide for high-performance electromagnetic interference shielding, Carbon 130 (2018) 59–68.

[23] Q. Zhao, K. Zhang, S. Zhu, H.Y. Xu, D.G. Cao, L.N. Zhao, R.H. Zhang, W.L. Yin, Review on the electrical resistance/conductivity of carbon fiber reinforced polymer, Appl. Sci. 9 (11) (2019).

[24] B.A. Newcomb, Processing, structure, and properties of carbon fibers, Compos. Appl. Sci. Manuf. 91 (2016) 262–282.

[25] J. Chen, J.M. Wu, H.Y. Ge, D. Zhao, C. Liu, X.F. Hong, Reduced graphene oxide deposited carbon fiber reinforced polymer composites for electromagnetic interference shielding, Compos. Appl. Sci. Manuf. 82 (2016) 141–150.

[26] Y.D. Wu, X.Y. Cheng, S.Y. Chen, B. Qu, R. Wang, D.X. Zhuo, L.X. Wu, In situ formation of a carbon nanotube buckypaper for improving the interlaminar properties of carbon fiber composites, Mater. Des. 202 (2021).

[27] R. Ding, Y. Sun, J. Lee, J.-D. Nam, J. Suhr, Enhancing interfacial properties of carbon fiber reinforced epoxy composites by grafting MXene sheets (Ti_2C), Compos. B Eng. 207 (2021).

[28] L.C. Ma, Y.Y. Zhu, P.F. Feng, G.J. Song, Y.D. Huang, H. Liu, J.X. Zhang, J.C. Fan, H. Hou, Z.H. Guo, Reinforcing carbon fiber epoxy composites with triazine derivatives functionalized graphene oxide modified sizing agent, Compos. B Eng. 176 (2019).

[29] H.B. Xu, X.Q. Zhang, D. Liu, C. Yan, X. Chen, D. Hui, Y.D. Zhu, Cyclomatrix-type polyphosphazene coating: improving interfacial property of carbon fiber/epoxy composites and preserving fiber tensile strength, Compos. B Eng. 93 (2016) 244–251.

[30] Y.J. Kwon, Y. Kim, H. Jeon, S. Cho, W. Lee, J.U. Lee, Graphene/carbon nanotube hybrid as a multi-functional interfacial reinforcement for carbon fiber-reinforced composites, Compos. B Eng. 122 (2017) 23–30.

[31] M. He, P. Xu, Y.J. Zhang, K.S. Liu, X.P. Yang, Phthalocyanine nanowires@GO/carbon fiber composites with enhanced interfacial properties and electromagnetic interference shielding performance, Chem. Eng. J. 388 (2020).

[32] V. Varshney, A.K. Roy, J.W. Baur, Modeling the role of bulk and surface characteristics of carbon fiber on thermal conductance across the carbon-fiber/matrix interface, ACS Appl. Mater. Interfaces 7 (48) (2015) 26674–26683.

[33] S. Jang, J. Kim, D.W. Kim, J.W. Kim, S. Chun, H.J. Lee, G.R. Yi, C. Pang, Carbon-based, ultraelastic, hierarchically coated fiber strain sensors with crack-controllable beads, ACS Appl. Mater. Interfaces 11 (16) (2019) 15079–15087.

[34] X.M. Chen, S.Y. Cheng, K.Q. Wen, C.J. Wang, J. Zhang, H. Zhang, H.C. Ma, L. Wu, T.L. Li, B.T. Li, J.Y. Shao, In-situ damage self-monitoring of fiber-reinforced composite by integrating self-powered ZnO nanowires decorated carbon fabric, Compos. B Eng. 248 (2023).

[35] G.M. Yang, X. Feng, W. Wang, Q. OuYang, L. Liu, Effective interlaminar reinforcing and delamination monitoring of carbon fibrous composites using a novel nano-carbon woven grid, Compos. Sci. Technol. 213 (2021).

[36] H. Zhang, Y. Liu, M. Kuwata, E. Bilotti, T. Peijs, Improved fracture toughness and integrated damage sensing capability by spray coated CNTs on carbon fibre prepreg, Compos. Appl. Sci. Manuf. 70 (2015) 102–110.

[37] Y. Yang, L. Shi, Z. Cao, R. Wang, J. Sun, Strain sensors with a high sensitivity and a wide sensing range based on a Ti3C2Tx (MXene) nanoparticle–nanosheet hybrid network, Adv. Funct. Mater. 29 (14) (2019), 1807882.

[38] Z.U.D. Babar, B. Della Ventura, R. Velotta, V. Iannotti, Advances and emerging challenges in MXenes and their nanocomposites for biosensing applications, RSC Adv. 12 (30) (2022) 19590–19610.

[39] V. Kedambaimoole, N. Kumar, V. Shirhatti, S. Nuthalapati, P. Sen, M.M. Nayak, K. Rajanna, S. Kumar, Laser-induced direct patterning of free-standing Ti3C2–MXene films for skin conformal tattoo sensors, ACS Sens. 5 (7) (2020) 2086–2095.

[40] K. Grabowski, S. Srivatsa, A. Vashisth, L. Mishnaevsky, T. Uhl, Recent advances in MXene-based sensors for Structural Health Monitoring applications: a review, Measurement 189 (2022).

[41] S. Srivatsa, P. Belthangadi, S. Ekambaram, M. Pai, P. Sen, T. Uhl, S. Kumar, K. Grabowski, M.M. Nayak, Dynamic response study of Ti3C2-MXene films to shockwave and impact forces, RSC Adv. 10 (49) (2020) 29147–29155.

[42] S.L. Chinke, I.S. Sandhu, D.R. Saroha, P.S. Alegaonkar, Graphene-like nanoflakes for shock absorption applications, ACS Appl. Nano Mater. 1 (11) (2018) 6027–6037.

[43] R. Ibragimova, P. Erhart, P. Rinke, H.-P. Komsa, Surface functionalization of 2D MXenes: trends in distribution, composition, and electronic properties, J. Phys. Chem. Lett. 12 (9) (2021) 2377–2384.

[44] J.-M. Cao, I.V. Zatovsky, Z.-Y. Gu, J.-L. Yang, X.-X. Zhao, J.-Z. Guo, H. Xu, X.-L. Wu, Two-dimensional MXene with multidimensional carbonaceous matrix: a platform for general-purpose functional materials, Prog. Mater. Sci. 135 (2023), 101105.

[45] K.R.G. Lim, M. Shekhirev, B.C. Wyatt, B. Anasori, Y. Gogotsi, Z.W. Seh, Fundamentals of MXene synthesis, Nature Synthesis 1 (8) (2022) 601–614.

[46] J.L. Hart, K. Hantanasirisakul, A.C. Lang, B. Anasori, D. Pinto, Y. Pivak, J.T. van Omme, S.J. May, Y. Gogotsi, M.L. Taheri, Control of MXenes' electronic properties through termination and intercalation, Nat. Commun. 10 (2019).

[47] V. Shukla, The tunable electric and magnetic properties of 2D MXenes and their potential applications, Materials Advances 1 (9) (2020) 3104–3121.

[48] L.X. Liu, W. Chen, H.B. Zhang, L.X. Ye, Z.G. Wang, Y. Zhang, P. Min, Z.Z. Yu, Super-tough and environmentally stable aramid Nanofiber@MXene coaxial fibers with outstanding electromagnetic interference shielding efficiency, Nano-Micro Lett. 14 (1) (2022).

[49] L.Z. Li, W.B. Liu, F. Yang, W.C. Jiao, L.F. Hao, R.G. Wang, Interfacial reinforcement of hybrid composite by electrophoretic deposition for vertically aligned carbon nanotubes on carbon fiber, Compos. Sci. Technol. 187 (2020).

[50] L. Bhanuprakash, S. Parasuram, S. Varghese, Experimental investigation on graphene oxides coated carbon fibre/epoxy hybrid composites: mechanical and electrical properties, Compos. Sci. Technol. 179 (2019) 134–144.

[51] A. Haghbin, G. Liaghat, H. Hadavinia, A.M. Arabi, M.H. Pol, Enhancement of the electrical conductivity and interlaminar shear strength of CNT/GFRP hierarchical composite using an electrophoretic deposition technique, Materials 10 (10) (2017).

[52] M.H. Islam, S. Afroj, M.A. Uddin, D.V. Andreeva, K.S. Novoselov, N. Karim, Graphene and CNT-based smart fiber-reinforced composites: a review, Adv. Funct. Mater. 32 (40) (2022).

[53] M. M, K.E.R. Roy, M.A. M, S.B.A. Hassan, A. Masihadas, Effect of EPD coated silanized graphene oxide on carbon fiber reinforced plastic: an emphasis on mechanical properties at cryogenic temperatures, Surf. Coating. Technol. 451 (2022), 129043.

[54] Y. Chae, S.J. Kim, S.Y. Cho, J. Choi, K. Maleski, B.J. Lee, H.T. Jung, Y. Gogotsi, Y. Lee, C.W. Ahn, An investigation into the factors governing the oxidation of two-dimensional Ti3C2 MXene, Nanoscale 11 (17) (2019) 8387–8393.

[55] A. Iqbal, F. Shahzad, K. Hantanasirisakul, M.K. Kim, J. Kwon, J. Hong, H. Kim, D. Kim, Y. Gogotsi, C.M. Koo, Anomalous absorption of electromagnetic waves by 2D transition metal carbonitride Ti_3CNT_x (MXene), Science 369 (6502) (2020) 446–+.

[56] L.R. Yao, M. Li, Q. Wu, Z.S. Dai, Y.Z. Gu, Y.X. Li, Z.G. Zhang, Comparison of sizing effect of T700 grade carbon fiber on interfacial properties of fiber/BMI and fiber/epoxy, Appl. Surf. Sci. 263 (2012) 326–333.

[57] Y. Li, H. Zhang, Y. Liu, H.S. Wang, Z.H. Huang, T. Peijs, E. Bilotti, Synergistic effects of spray-coated hybrid carbon nanoparticles for enhanced electrical and thermal surface conductivity of CFRP laminates, Compos. Appl. Sci. Manuf. 105 (2018) 9–18.

[58] M.H. Al-Saleh, U. Sundararaj, Electromagnetic interference shielding mechanisms of CNT/polymer composites, Carbon 47 (7) (2009) 1738–1746.

[59] M. Bayat, H. Yang, F.K. Ko, D. Michelson, A. Mei, Electromagnetic interference shielding effectiveness of hybrid multifunctional Fe3O4/carbon nanofiber composite, Polymer 55 (3) (2014) 936–943.

[60] H. Zhao, L. Hou, S.Y. Bi, Y.X. Lu, Enhanced X-band electromagnetic-interference shielding performance of layer-structured fabric-supported polyaniline/cobalt-nickel coatings, ACS Appl. Mater. Interfaces 9 (38) (2017) 33059–33070.

[61] A. Sarycheva, Y. Gogotsi, Raman spectroscopy analysis of the structure and surface chemistry of $Ti_3C_2T_x$ MXene, Chem. Mater. 32 (8) (2020) 3480–3488.

[62] W. Sun, S.A. Shah, Y. Chen, Z. Tan, H. Gao, T. Habib, M. Radovic, M.J. Green, Electrochemical etching of Ti_2AlC to Ti_2CT_x (MXene) in low-concentration hydrochloric acid solution, J. Mater. Chem. A 5 (41) (2017) 21663–21668.

[63] X.R. Gao, B.B. Wang, K.K. Wang, S. Xu, S.P. Liu, X.H. Liu, Z.R. Jia, G.L. Wu, Design of Ti3C2Tx/TiO2/PANI multi-layer composites for excellent electromagnetic wave absorption performance, J. Colloid Interface Sci. 583 (2021) 510–521.

[64] C.B. Liang, H. Qiu, P. Song, X.T. Shi, J. Kong, J.W. Gu, Ultra-light MXene aerogel/wood-derived porous carbon composites with wall-like "mortar/brick" structures for electromagnetic interference shielding, Sci. Bull. 65 (8) (2020) 616–622.

[6][5]] J. Halim, K.M. Cook, M. Naguib, P. Eklund, Y. Gogotsi, J. Rosen, M.W. Barsoum, X-ray photoelectron spectroscopy of select multi-layered transition metal carbides (MXenes), Appl. Surf. Sci. 362 (2016) 406–417.

[66] T. Sun, M.X. Li, S.T. Zhou, M. Liang, Y. Chen, H.W. Zou, Multi-scale structure construction of carbon fiber surface by electrophoretic deposition and electropolymerization to enhance the interfacial strength of epoxy resin composites, Appl. Surf. Sci. 499 (2020).

[67] Q. Wu, J.Q. He, F. Wang, X. Yang, J.F. Zhu, Constructing a simple anti-sandwich structure on carbon fiber surface for simultaneously strengthening and toughening the interphase of epoxy composites, Compos. Struct. 240 (2020).

[68] A. Lipatov, H.D. Lu, M. Alhabeb, B. Anasori, A. Gruverman, Y. Gogotsi, A. Sinitskii, Elastic properties of 2D $Ti_3C_2T_x$ MXene monolayers and bilayers, Sci. Adv. 4 (6) (2018).

[69] P.K. Gangineni, S. Yandrapu, S.K. Ghosh, A. Anand, R.K. Prusty, B.C. Ray, Mechanical behavior of Graphene decorated carbon fiber reinforced polymer composites: an assessment of the influence of functional groups, Compos. Appl. Sci. Manuf. 122 (2019) 36–44.

[70] S. De, A.O. Fulmali, K.C. Nuli, R.K. Prusty, B.G. Prusty, B.C. Ray, Improving delamination resistance of carbon fiber reinforced polymeric composite by interface engineering using carbonaceous nanofillers through electrophoretic deposition: an assessment at different in-service temperatures, J. Appl. Polym. Sci. 138 (15) (2021).

[71] S.B. De, A.O. Fulmali, P.N. Shivangi, S. Choudhury, R.K. Prusty, B.C. Ray, Interface modification of carbon fiber reinforced epoxy composite by hydroxyl/carboxyl functionalized carbon nanotube, Mater. Today Proc. 27 (2020) 1473–1478.

[72] X. Sui, J. Shi, H. Yao, Z. Xu, L. Chen, X. Li, M. Ma, L. Kuang, H. Fu, H. Deng, Interfacial and fatigue-resistant synergetic enhancement of carbon fiber/epoxy hierarchical composites via an electrophoresis deposited carbon nanotube-toughened transition layer, Compos. Appl. Sci. Manuf. 92 (2017) 134–144.

[73] A. Yadav, B.A. Nayak, A.O. Fulmali, R.K. Prusty, Synergetic impact of both fiber surface grafting and matrix modification by carbon nanotubes and functionalized carbon nanotubes on the flexural behavior of carbon fiber reinforced polymer composites: an assessment at cryo-, room-, and elevated- in situ temperature conditions, J. Appl. Polym. Sci. 139 (45) (2022), e53104.

[74] P.G. He, B.Y. Huang, L. Liu, Q. Huang, T.F. Chen, Preparation of multiscale graphene oxide-carbon fabric and its effect on mechanical properties of hierarchical epoxy resin composite, Polym. Compos. 37 (5) (2016) 1515–1522.

[75] Y. Hu, S. Pang, J. Li, J. Jiang, D.G. Papageorgiou, Enhanced interfacial properties of hierarchical MXene/CF composites via low content electrophoretic deposition, Compos. B Eng. 237 (2022), 109871.

[76] C.F. Han, S.W. Huang, B.Z. Sun, B.H. Gu, Electrical resistance changes of 3D carbon fiber/epoxy woven composites under short beam shear loading along different orientations, Compos. Struct. 276 (2021).

[77] L. Zhang, Y. Chen, Q. Liu, W. Deng, Y. Yue, F. Meng, Ultrathin flexible electrospun carbon nanofibers reinforced graphene microgasbags films with three-dimensional conductive network toward synergetic enhanced electromagnetic interference shielding, J. Mater. Sci. Technol. 111 (2022) 57–65.

[78] D. Micheli, A. Vricella, R. Pastore, M. Marchetti, Synthesis and electromagnetic characterization of frequency selective radar absorbing materials using carbon nanopowders, Carbon 77 (2014) 756–774.

[79] X. Li, X. Yin, C. Song, M. Han, H. Xu, W. Duan, L. Cheng, L. Zhang, Self-assembly core-shell graphene-bridged hollow MXenes spheres 3D foam with ultrahigh specific EM absorption performance, Adv. Funct. Mater. 28 (2018), 180393841.

[80] J.M. Wu, J. Chen, Y.Y. Zhao, W.X. Liu, W.B. Zhang, Effect of electrophoretic condition on the electromagnetic interference shielding performance of reduced graphene oxide-carbon fiber/epoxy resin composites, Compos. B Eng. 105 (2016) 167–175.

[81] H.J. Duan, M.J. Zhao, Y.Q. Yang, G.Z. Zhao, Y.Q. Liu, Flexible and conductive PP/EPDM/Ni coated glass fiber composite for efficient electromagnetic interference shielding, J. Mater. Sci. Mater. Electron. 29 (12) (2018) 10329–10336.

[82] Y. Yang, M.C. Gupta, K.L. Dudley, R.W. Lawrence, A comparative study of EMI shielding properties of carbon nanofiber and multi-walled carbon nanotube filled polymer composites, J. Nanosci. Nanotechnol. 5 (6) (2005) 927–931.

[83] J. Chen, D. Zhao, H.Y. Ge, J. Wang, Graphene oxide-deposited carbon fiber/cement composites for electromagnetic interference shielding application, Construct. Build. Mater. 84 (2015) 66–72.

[84] X.D. Gao, W.M. Yang, L.S. Cheng, Y.M. Ding, J. Zhan, J. Tan, Epoxy resin composite containing nanocarbon-coated glass fiber and cloth for electromagnetic interference shielding, J. Mater. Res. Technol. 13 (2021) 1759–1766.

[85] N. Yesmin, V. Chalivendra, Electromagnetic shielding effectiveness of glass fiber/epoxy laminated composites with multi-scale reinforcements, Journal of Composites Science 5 (8) (2021).

[86] M.S. Hong, W.K. Choi, K.H. An, S.J. Kang, S.J. Park, Y.S. Lee, B.J. Kim, Electromagnetic interference shielding behaviors of carbon fibers-reinforced polypropylene matrix composites: II. Effects of filler length control, J. Ind. Eng. Chem. 20 (5) (2014) 3901–3904.

[87] J.A. Rojas, L.F.D. Santos, E.C. Botelho, B. Ribeiro, M.C. Rezende, Morphological, mechanical, and electromagnetic interference shielding effectiveness characteristics of glass fiber/epoxy resin/MWCNT buckypaper composites, J. Appl. Polym. Sci. 138 (25) (2021).

[88] M. Paligová, J. Vilčáková, P. Sáha, V. Křesálek, J. Stejskal, O. Quadrat, Electromagnetic shielding of epoxy resin composites containing carbon fibers coated with polyaniline base, Phys. Stat. Mech. Appl. 335 (3) (2004) 421–429.

[89] S. Joon, R. Kumar, A.P. Singh, R. Shukla, S.K. Dhawan, Lightweight and solution processible thin sheets of poly(o-toluidine)-carbon fiber-novolac composite for EMI shielding, RSC Adv. 5 (68) (2015) 55059–55065.